Supporting Information

Dual-Parameter Self-Calibrating Probes for Organelle Polarity by Decoupling Viscosity from Polarity

Lei Huang[a], Chuanhao Liu[b], Wenxiao Deng[a], Yuchang Tan[a], Yanfei Tan[c]*, and Yan Huang[a]*

a. Key Laboratory of Green Chemistry and Technology (Ministry of Education), College of Chemistry, Sichuan University, Chengdu, Sichuan, 610064, China; E-mail: huangyan@scu.edu.cn.

b. Analytical & Testing Center, Sichuan University, Chengdu, 610064,China.

c. National Engineering Research Center for Biomaterials and College of Biomedical Engineering, Sichuan University, Chengdu, 610064 (P. R. China). E-mail: tanyf@scu.edu.cn.

Table of contents

Dual-Parameter Self-Calibrating Probes for Organelle Polarity by Decoupling Viscosity from Polarity

1. Experimental procedures

1.1 General information.

Materials. Unless stated otherwise, all reagents and anhydrous solvents were purchased from *Bidepharm* and *Adamas-beta*. Dulbecco's modified Eagle's medium (DMEM), phosphate-buffered saline (PBS), fetal bovine serum (FBS) and Buffer solutions (pH = 1-13) were purchased from Grand Island Biological Compan. Mitochondrial tracker and lysosomal tracker were purchased from Shanghai Biyuntian Biotechnology. The ROS detection kit (DCFH probe) was purchased from Shanghai Macklin Biochemical Technology.

Measurement and Instruments. ^{1}H NMR and ^{13}C NMR spectra were acquired on a Bruker Avanced II-400 MHz spectrometer at 400 and 100 MHz in $CDCl_3$, respectively. Tetramethylsilane (TMS) was utilized as an internal standard. High-resolution MS spectra were obtained via a Q-TOF Premier ESI mass spectrometer (Micromass, Manchester, UK). UV-Vis absorption spectra were obtained on a UV-VIS A590 spectrophotometer (AOELAB Ltd). Steady-state photoluminescence (PL) emission spectra were recorded on a Horiba Jobin Yvon Fluoromax+ fluorescence spectrophotometer. The absolute PL quantum yield (PLQY) of the **DT-NIN**, **DT-NIO** and **DT-NINI** were determined on a HORIBA Jobin Yvon Fluorolog-3 fluorescence spectrometer equipped with an integrating sphere (IS80 from Labsphere) and a digital photometer (S370 from UDT) under ambient conditions. The crystallographic data for **DT-NIN** reported here have been deposited in the Cambridge Structural Database (CCDC:2530395). Single crystal X-ray diffraction data of **DT-NIN** were obtained on a Bruker APEX-II CCD diffractometer equipped with a graphite monochromator MoKα (λ = 0.71073 Å) radiation. Using Olex2, the structures were solved with the SHELXT structure solution program using Intrinsic Phasing and refined with the SHELXL refinement package using Least Squares minimization. The concentration of solution samples for photophysical measurements was 1×10^{-5} mol·L^{-1}. Cellular imaging experiments were performed with a confocal laser scanning microscope (LSM 880 with Airyscan, Zeiss, Germany).

Computational Methods Details. Theoretical computations were performed using the Gaussian 09 software packages. Based on the single-crystal

structure, the ground state was optimized using density functional theory (DFT), and the excited state was optimized employing time-dependent density functional theory (TD-DFT) using the B3LYP hybrid functional and 6-31G(d) basis. The electrostatic potential involved in the analyses was evaluated by Multiwfn based on the highly effective algorithm proposed in Ref[1].

Cell Culture. All the cell lines were kindly provided by National Research Center for Biomaterials, Sichuan University. 4T1, L929 and MSC cells were cultured in DMEM medium supplemented with 10% fetal bovine serum and 1% antibiotics at 37 °C and 5 % CO_2.

Cell viability assay. The cell cytotoxicity of **DT-NIN**, **DT-NIN**I and **DT-NIO** to living L929 cells was assessed using a standard CCK-8 assay (cell counting kit-8). About 1 × 10^4 cells/well in 100 μL cell culture medium were seeded in a 96-well microplate. The medium was then replaced with fresh medium containing **DT-NIs** Compound at various concentrations of 0 μM, 5 μM, 10 μM, 20 μM and 40 μM for 24 h. Subsequently, the cells were washed with fresh medium three times, and 10 μL CCK-8 in 90 μL PBS was added to each well for another 1 h. The absorbance was measured using an ELISA microplate reader at a wavelength of 450 nm. Cell viability was expressed relative to the control group, which was considered to have 100% metabolic activity.

Flow cytometric analysis. while L929 cells were seeded in 6-well plate for 24 hours, the culture medium was replaced by **DT-NIN**, **DT-NINI** or **DT-NIO** (10 μM) for 3 h, then the cells were collected for flow cytometric detection.

Colocalization Studies. L929 cells were seeded in confocal culture dishes at a density of 1×10^4 cells per well with 1 mL of culture medium and incubated overnight to allow for adherence. Subsequently, the cells were incubated with culture medium containing **DT-NIN** (10 μM), **DT-NIO** (10 μM), or **DT-NINI** (10 μM) for 3 h. Upon completion of the incubation, the medium was removed, and the cells were washed three times with PBS. The cells were then co-stained with Lyso-Tracker or Mito-Tracker for 30min. Fluorescence images were acquired using a confocal laser scanning microscope (CLSM) with the following parameters: for Lyso-Tracker ($\lambda_{ex}/\lambda_{em}$ = 543/548–650 nm); for Mito-Tracker ($\lambda_{ex}/\lambda_{em}$ = 633/638–759 nm); and for the **DT-NIs** series ($\lambda_{ex}/\lambda_{em}$ = 405/600–740 nm).

Intracellular spectral detection. Three cells, 4T1，L929 and human mesenchymal stem cells (MSCs) were applied in this part. Different cells were seeded on a confocal dish with 1 × 10^4 cells per dish and 1 mL medium overnight. Then, cells were incubated with culture medium containing **DT-NIs** (10 μM for **DT-NIN, DT-NIO** and **DT-NINI**) for 3 h. After that, the medium was removed, and the cells were washed 3 times with PBS. A series of Fluorescence images were obtained by CLSM under following parameters (λ_{ex} = 405 nm, λ_{em} from 412 nm to 722 nm, per 5 nm). Then, the fluorescent spectral in different cells were obtained according to the intensity of these photographs.

In Vitro Total Reactive Oxygen Species (ROS) Detection. The ROS generation capability was evaluated using 2′,7′-dichlorodihydrofluorescein (DCFH) as the indicator. Briefly, to prepare the DCFH stock solution, a solution of DCFH-DA in DMSO (0.25 mL, 0.5 mg/mL) was mixed with NaOH solution (1 mL, 10 mM) and incubated in the dark for 30 min to hydrolyze the ester bonds. The hydrolysate was then diluted with PBS (50 mM, 5 mL). For the ROS generation assay, an aliquot of the prepared DCFH solution (40 μM, 200 μL) was added to a DMSO solution (800 μL) containing the photosensitizer (**DT-NINI**, **DT-NIO**, or **DT-NIN,** 1×10^{-5} M). The mixture was irradiated using an 800-lumen white light source for varying durations. The rate of ROS generation was determined by monitoring the fluorescence emission intensity of DCFH in the range of 500–600 nm. A blank control containing only the DCFH solution without photosensitizers was subjected to identical experimental conditions. Mechanistically, non-fluorescent DCFH is oxidized by ROS to form the highly fluorescent 2′,7′-dichlorofluorescein (DCF), resulting in an emission signal at 500-600 nm that is proportional to the environmental ROS level.

1.2 Synthesis of DT-NIs

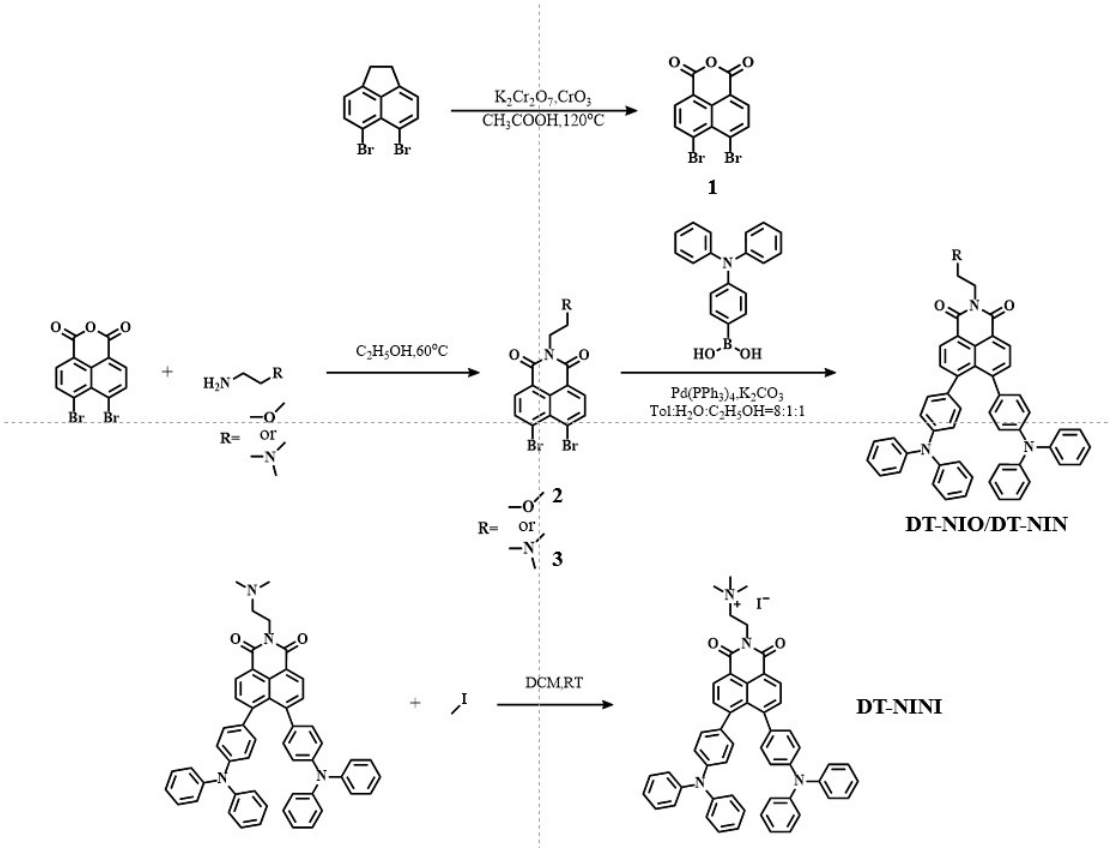

Scheme S1. The synthetical routs of **DT-NIs**.

4,5-dibromonaphthalene-1,8-dicarboxylic acid (1)

5,6-Dibromo-1,2-dihydroacenaphthylene (1.04 g, 3.20 mmol), potassium dichromate (5.6 g, 19.2 mmol), and chromium trioxide (960 mg, 9.60 mmol) were dissolved in 30 mL of glacial acetic acid. The mixture was heated at 120 °C under reflux for 12 h. During the reaction, the solution color gradually changed from orange-red to a green suspension. Upon completion, the mixture was poured into ice water and filtered under vacuum to collect a green solid. The crude product was washed with concentrated HCl to yield a light pink solid, followed by washing with dichloromethane (DCM) to afford target compound **1** (959 mg, 2.69 mmol, 84%). Due to its extremely poor solubility, no further characterization was performed for this compound.

6,7-dibromo-2-(2-methoxyethyl)-1*H*-benzo[*de*]isoquinoline-1,3(2*H*)-dione (2)

Compound **1** (356 mg, 1 mmol) was charged into a 150 mL three-necked flask

containing 30 mL of ethanol. After refluxing at 60 °C under an argon atmosphere for 30 min, 2-methoxyethan-1-amine (150 mg) was added. The reaction was maintained for 2.5 h. The mixture was then filtered, and the solvent was removed under reduced pressure. The residue was purified by silica gel column chromatography to yield target compound **2** (80 mg, 0.19 mmol, 19%). ^{1}H NMR (400 MHz, $CDCl_3$) δ (ppm): 8.41 (d, J = 7.4 Hz, 2H), 8.21 (d, J = 7.4 Hz, 2H), 4.41 (d, J = 5.6 Hz, 2H), 3.72 (d, J = 5.6 Hz, 2H), 3.36 (s, 2H).

6,7-dibromo-2-(2-(dimethylamino)ethyl)-1*H*-benzo[*de*]isoquinoline-1,3(2*H*)-dione (3)

Compound **1** (356 mg, 1 mmol) was charged into a 150 mL three-necked flask with 30 mL of ethanol. After refluxing at 60 °C under argon for 30 min, 2-(dimethylamino)ethan-1-amine (176 mg) was added. The reaction proceeded for 2.5 h. After filtration and evaporation of the solvent, the crude product was purified by column chromatography to afford target compound **3** (74 mg, 0.17 mmol, 17%). ^{1}H NMR (400 MHz, $CDCl_3$) δ (ppm): 8.40 (d, J = 8.0 Hz, 2H), 8.21 (d, J = 8.0 Hz, 2H), 4.35 (d, J = 6.84 Hz, 2H), 3.72 (s, 2H), 3.36 (s, 6H).

6,7-bis(4-(diphenylamino)phenyl)-2-(2-methoxyethyl)-1*H*-benzo[*de*]isoquinoline-1,3(2*H*)-dione (DT-NIO)

Compound **2** (75 mg, 0.18 mmol), 4-(diphenylamino)phenylboronic acid (115 mg, 0.40 mmol), $Pd(PPh_3)_4$ (10 mg, 0.01 mmol), and K_2CO_3(100 mg, 0.73 mmol) were added to a 50 mL Schlenk tube. Toluene/ethanol/H_2O (8 mL/1 mL/1 mL) was used as the solvent. The system was degassed and backfilled with argon. The reaction was stirred at 100 °C for 12 h. The target compound was isolated as an orange solid (63 mg, 0.085 mmol, 47%) via silica gel column chromatography. ^{1}H NMR (400 MHz, $CDCl_3$) δ (ppm): 8.68 (d, J = 7.6 Hz, 2H), 7.70 (d, J = 7.6 Hz, 2H), 7.24 (t, J_1 = 7.3 Hz, J_2 = 7.2 Hz, 8H), 7.17 (d, J = 7.3 Hz, 8H), 7.06 (t, J = 7.2 Hz, 4H), 6.89 (d, J = 8.7 Hz, 4H), 6.85 (d, J = 8.7 Hz, 4H), 4.49 (t, J = 5.9 Hz, 2H), 3.77 (t, J = 5.9 Hz, 2H), 3.40 (s, 3H). ^{13}C NMR (100 MHz, $CDCl_3$) δ (ppm): 164.5, 147.7, 147.3 147.0, 134.9, 130.84, 130.75, 130.5, 129.4, 128.0, 125.4, 123.6, 121.3, 120.6, 77.2, 69.7, 58.9, 39.3. HRMS (ESI) m/z: $[M + H]^+$ calcd. for $C_{51}H_{40}N_3O_3^+$, 742.3064; found, 742.3061.

6,7-bis(4-(diphenylamino)phenyl)- 2-(2-(dimethylamino)ethyl)-1*H*-benzo[*de*]isoquinoline-1,3(2*H*)-dione (DT-NIN)

Compound **3** (84 mg, 0.20 mmol), 4-(diphenylamino)phenylboronic acid (127 mg, 0.44 mmol), $Pd(PPh_3)_4$ (12 mg, 0.01 mmol), and K_2CO_3 (111 mg, 0.80 mmol) were added to a 50 mL Schlenk tube. Toluene/ethanol/H_2O (8 mL/1 mL/1 mL) was used as the solvent. After degassing and purging with argon, the mixture was heated at 100 °C for 12 h. Purification by column chromatography afforded the target compound as an orange solid (70 mg, 0.09 mmol, 46%). ^{1}H NMR (400 MHz, $CDCl_3$) *δ* (ppm): 8.67 (d, *J* = 7.7 Hz, 2H), 7.70 (d, *J* = 7.7 Hz, 2H), 7.21 (t, J_1 = 7.3 Hz, J_2 = 7.2 Hz, 8H), 7.17 (d, *J* = 7.3 Hz, 8H), 7.05 (t, *J* = 7.2 Hz, 4H), 6.89 (d, *J* = 8.7 Hz, 4H), 6.85 (d, *J* = 8.73 Hz, 4H), 4.42 (t, *J* = 6.7 Hz, 2H), 2.80 (t, *J* = 6.7 Hz, 2H), 2.46 (s, 6H). ^{13}C NMR (100 MHz, $CDCl_3$) *δ* (ppm): 164.5, 147.7, 147.3 147.0, 134.8, 130.81, 130.77, 130.5, 129.4, 128.0, 125.4, 123.6, 121.3, 120.6, 77.2, 56.8, 45.5, 37.7. HRMS (ESI) m/z: $[M + H]^+$ calcd. for $C_{52}H_{43}N_4O_2^+$, 755.3381; found, 755.3380.

2-(6,7-bis(4-(diphenylamino)phenyl)-1,3-dioxo-1*H*-benzo[*de*]isoquinolin-2(3*H*)-yl)-N,N,N-trimethylethan-1-aminium iodide (DT-NINI)

DT-NIN (50 mg, 0.07 mmol) and methyl iodide (11 mg, 0.08 mmol) were dissolved in 10 mL of DCM in a 25 mL round-bottom flask. The mixture was stirred at room temperature under argon for 12 h. After the reaction, the solvent was evaporated. The resulting solid was washed with 30 mL of diethyl ether, filtered, and dried to yield the target compound as a dark red solid (45 mg, 0.05 mmol, 72%). ^{1}H NMR (400 MHz, $CDCl_3$) δ (ppm): 8.61 (d, *J* = 7.5 Hz, 2H), 7.68 (d, *J* = 7.5 Hz, 2H), 7.22 (t, J_1 = 7.5 Hz, J_2 = 7.3 Hz, 8H), 7.14 (d, *J* = 7.5 Hz, 8H), 7.04 (t, *J* = 7.3 Hz, 4H), 6.80 (s, 8H), 4.73 (t, *J* = 6.7 Hz, 2H), 4.11 (t, *J* = 6.7 Hz, 2H), 3.70 (s, 9H). ^{13}C NMR (100 MHz, $CDCl_3$) *δ* (ppm): 164.3, 148.8, 147.2, 147.1, 134.3, 131.5, 130.93, 130.85, 130.5, 129.5, 128.0, 123.7, 123.6, 120.5, 120.1, 77.3, 64.6, 54.7. HRMS (ESI) m/z: $[M]^+$ calcd. for $C_{53}H_{45}N_4O_2^+$, 769.3537; found, 769.3514.

2. Results and Discussion

2.1 Summary of Polarity Probes.

Table S1. Comparison of polarity fluorescent probes with $K_{\lambda E}$.

Probe	$K_{\lambda E}$	Reference
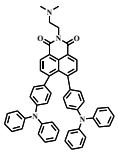 **DT-NIN**	17.2	This work
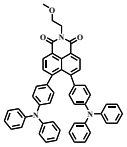 **DT-NIO**	16.5	This work
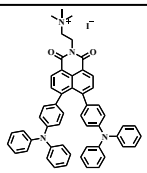 **DT-NINI**	16.9	This work
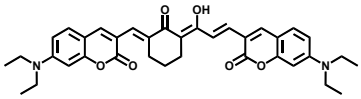 CC-CH	5.59	*Molecules*. **2023**, *28*, 6626.
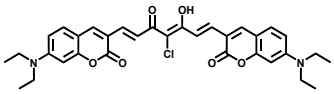 CC-Cl	5.27	*Molecules*. **2023**, *28*, 6626.
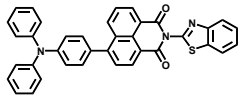 TPA-NDI-1	14.14	*Dyes and Pigments*. **2023**, 211, 111082
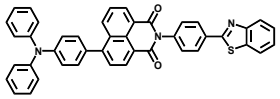 TPA-NDI-2	12.60	*Dyes and Pigments*. **2023**, 211, 111082
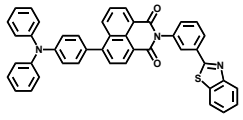 TPA-NDI-3	12.71	*Dyes and Pigments*. **2023**, 211, 111082
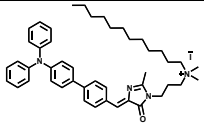 TICT-lipid	9.60	*Analytical Chemistry*. **2022** *94* (7), 3303-3312

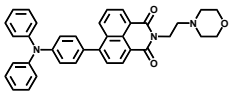 MND-Lys	9.40	*Chemical. Communications.* **2019**,55, 11063-11066
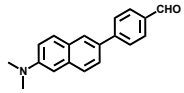 LDs-TPFP	11.98	*Analytica Chimica Acta*. **2020**,1136,34-41
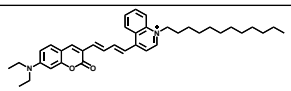 MTCQ	5.352	*Sensors and Actuators B: Chemical.* **2026**,448, 139027
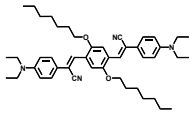 LD-DCDSB	6.52	*Analytical Chemistry.* **2025** 97 (43), 24176-24186
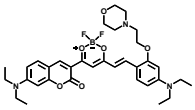 Lyso-BF	5.929	*Analytical Chemistry.* **2025** 97 (31), 17102-17110
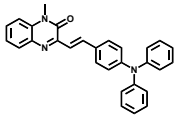 TPALD	8.750	*New Journal of Chemistry*. **2025**,49,9226-9232
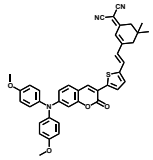 TPC-AN	8.188	*Analytica Chimica Acta.* **2025**,1352,343916
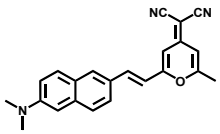 E4-BH	11	*Microchemical Journal.* **2025**,211,113018
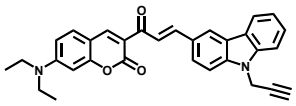 COB2	3.60	*Spectrochimica Acta Part A: Molecular and Biomolecular Spectroscopy.* **2025**,328,125455
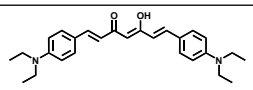 CN	6.85	*Journal of Materials Chemistry B.* **2023**,11,10836-10844
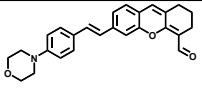 LD-H-Lyso	11.77	*Dyes and Pigments.* **2023**,208,110874

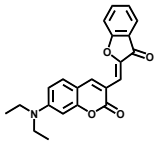 LD-CK	3.98	*Sensors and Actuators B: Chemical.* **2025**,426,137141
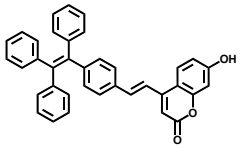 TPEC-DNBS	4.7165	*Analytica Chimica Acta.* **2025**,1334,343425
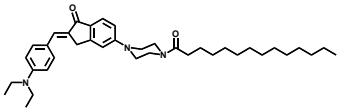 GA-P	4.4075	*Sensors and Actuators B: Chemical.* **2024**,419,136349
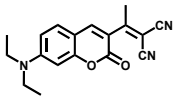 Cou-CN	3.16572	*Photochemical & Photobiological Sciences.* **2024**,23,1883-1891
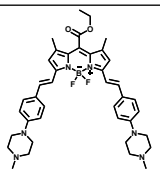 SNL	3.410	*Analytical Chemistry.* **2024** 96 (34), 14053-14059
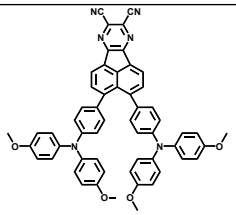 P-DOTPA	30.2	*Chemical Communications.* **2025**,61,10134-10137
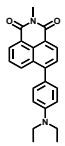 4	16.5	*Advanced Science.* **2025**,e08792
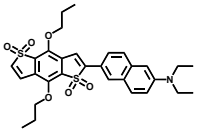 10	19.3	*Advanced Science.* **2025**,e08792
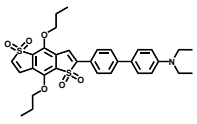 11	27.1	*Advanced Science.* **2025**,e08792

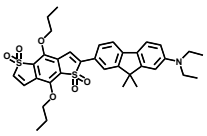 12	25.6	*Advanced Science.* **2025**,e08792
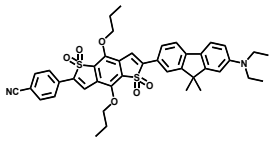 Lipi-PS	29.8	*Advanced Science.* **2025**,e08792

2.2 Single crystal and theoretical characterization

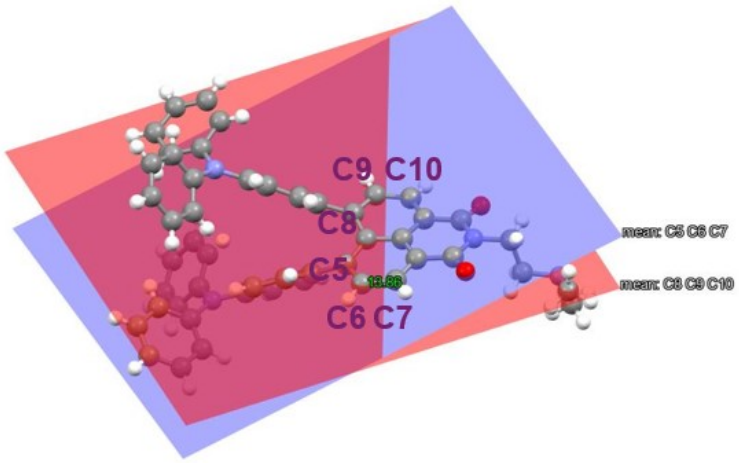

Figure S1. Distortion of the naphthalene core in the single crystals of **DT-NIN**.

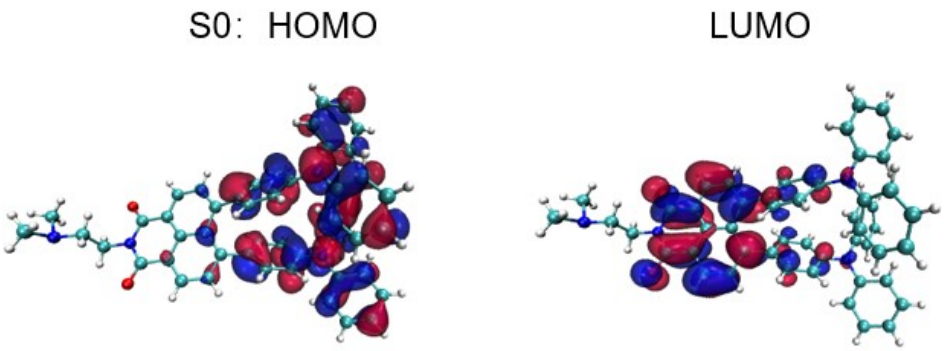

Figure S2. The S_0 orbital distributions of HOMO and LUMO in **DT-NIN**.

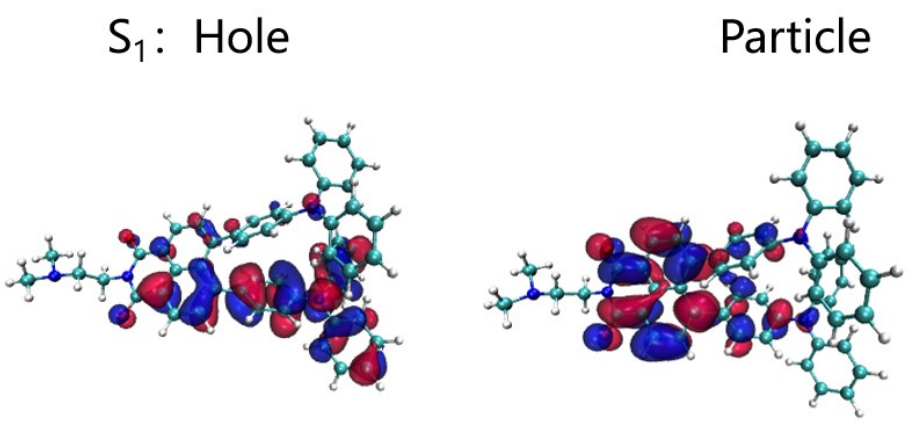

Figure S3. The S_1 orbital distributions of hole and particle in **DT-NIN**.

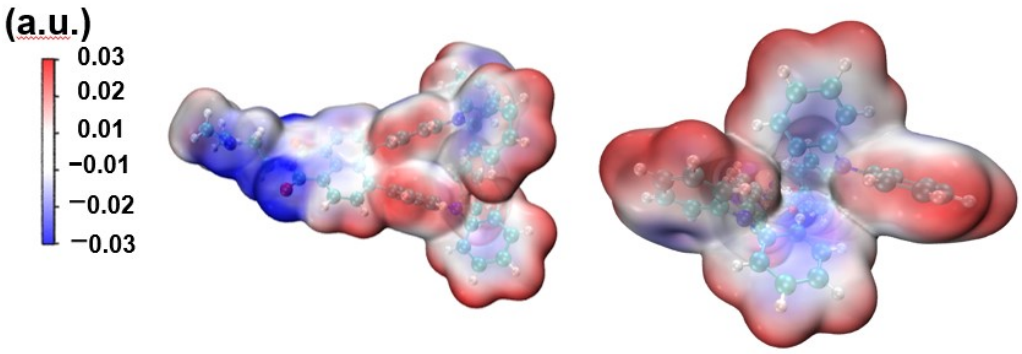

Figure S4. The ESP map of **DT-NIN** mapped on the electron density iso-surface.

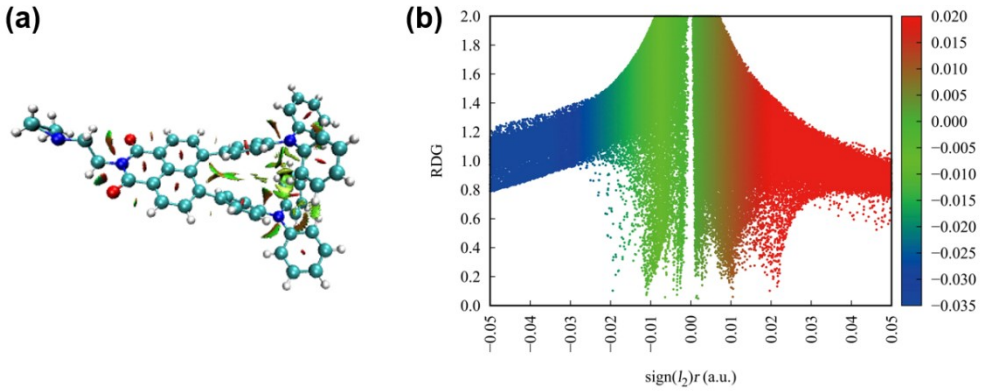

Figure S5. (a) The distribution of reduced density gradient (RDG) isosurface of **DT-NIN**; and (b) the scatter plot of RDG versus sign $(\lambda_2)r$ of **DT-NIN** in its S_1 state.

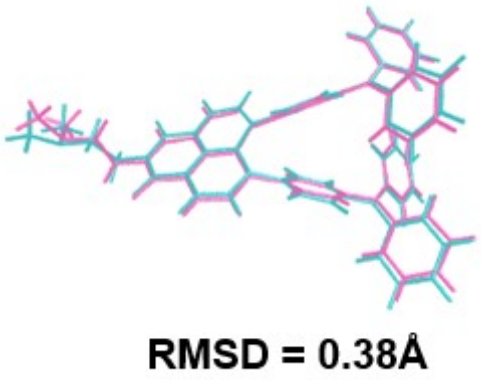

Figure S6. RMSD between the S_0 and the S_1 states of **DT-NIN**.

2.3 Photophysical characterization

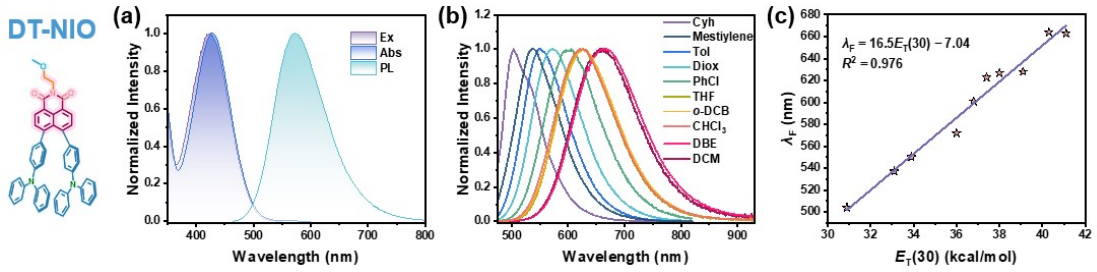

Figure S7. Polarity sensitivity of **DT-NIO**. (a) Excitation, absorption and PL spectra of **DT-NIO** in Diox (λ_{ex} = 430 nm, 1×10^{-5} M). (b) PL spectra of **DT-NIO** in different solvents. (c) Linear correlation between λ_F of **DT-NIO** and the empirical solvent parameter $E_T(30)$.

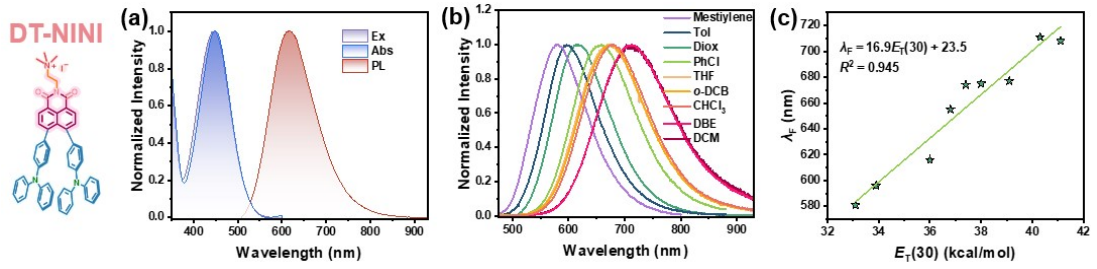

Figure S8. Polarity sensitivity of **DT-NINI**. (a) Excitation, absorption and PL spectra of **DT-NINI** in Diox (λ_{ex} = 430 nm, 1×10^{-5} M). (b) PL spectra of **DT-NINI** in different solvents. (c) Linear correlation between λ_F of **DT-NINI** and the empirical solvent parameter $E_T(30)$.

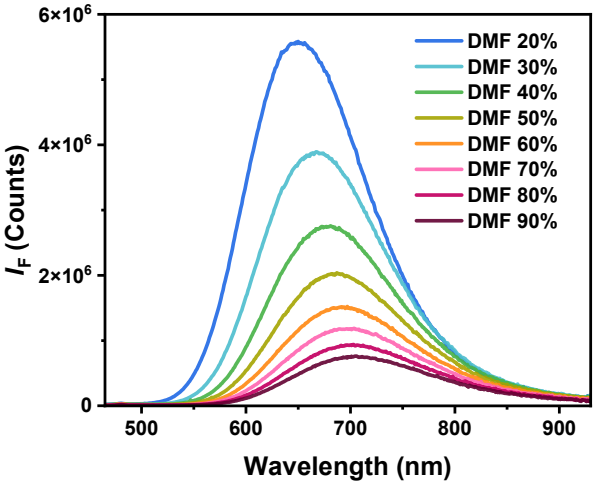

Figure S9. The PL spectrum of **DT-NIO** (1×10^{-5} M, λ_{ex} = 430 nm) in Diox-DMF mixtures.

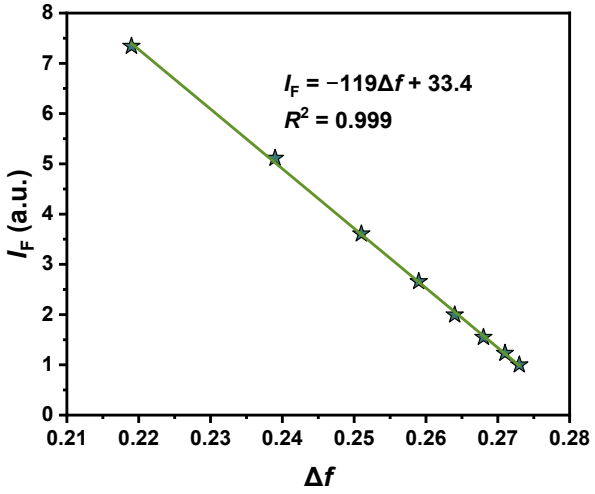

Figure S10. The linear relationship between the I_F of **DT-NIO** in Diox-DMF mixtures and corresponding **Δ*f***.

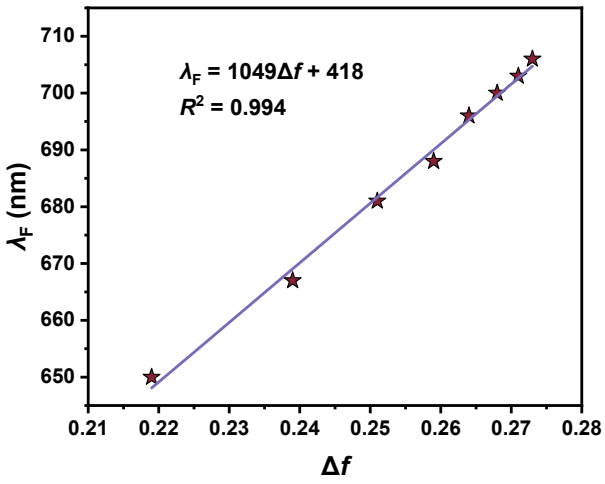

Figure S11. The linear relationship between the λ_F of **DT-NIO** in Diox-DMF mixtures and corresponding **Δ*f***.

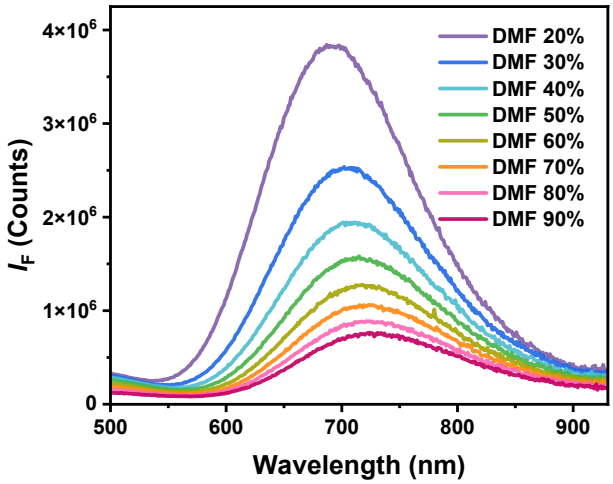

Figure S12. The PL spectrum of **DT-NINI** (1×10^{-5} M, λ_{ex} = 430 nm) in Diox-DMF mixtures.

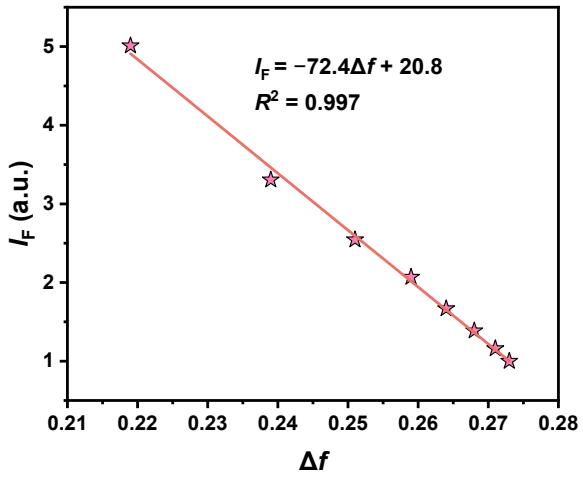

Figure S13. The linear relationship between the I_F of **DT-NINI** in Diox-DMF mixtures and corresponding **Δ*f***.

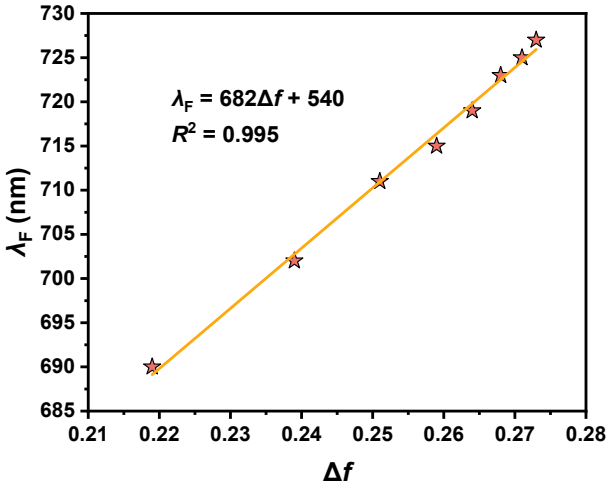

Figure S14. The linear relationship between the λ_F of **DT-NINI** in Diox-DMF mixtures and corresponding **Δ*f***.

Table S2. Viscosity of methanol–glycerol mixture.

NO.	Glycerol (mL)	methanol (mL)	Viscosity
1	150 mL	0 mL	1450 cP
2	150 mL	10 mL	880 cP
3	150 mL	20 mL	528 cP

4	150 mL	30 mL	323 cP
5	150 mL (80% Gly)	37.5 mL	272 cP
6	150 mL	50 mL	195 cP
7	150 mL	75 mL	144 cP
8	150 mL	100 mL	115 cP
9	150 mL	150 mL	83 cP
10	50 mL (20% Gly)	100 mL	9.60 cP

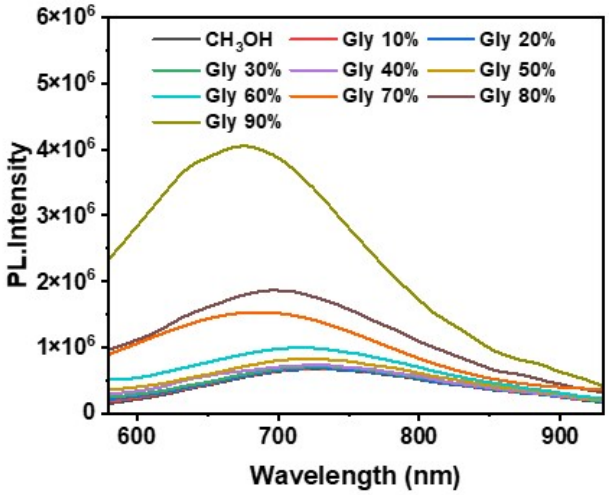

Figure S15. PL spectra of **DT-NIN** in methanol/glycerol mixtures with glycerol different fractions.

As depicted in Figure S15, under such a high glycerol content (90 vol% glycerol，viscosity: ~ 600 cP), the increase in PL intensity relative to that in pure methanol is less than 10-fold.

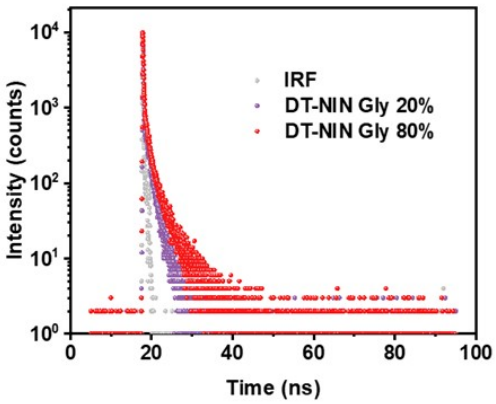

Figure S16. PL decay curves of **DT-NIN** in methanol/glycerol mixtures with glycerol fraction of 20% and 80%, respectively. (λ_{ex} = 405 nm; λ_{em} = 700 nm)

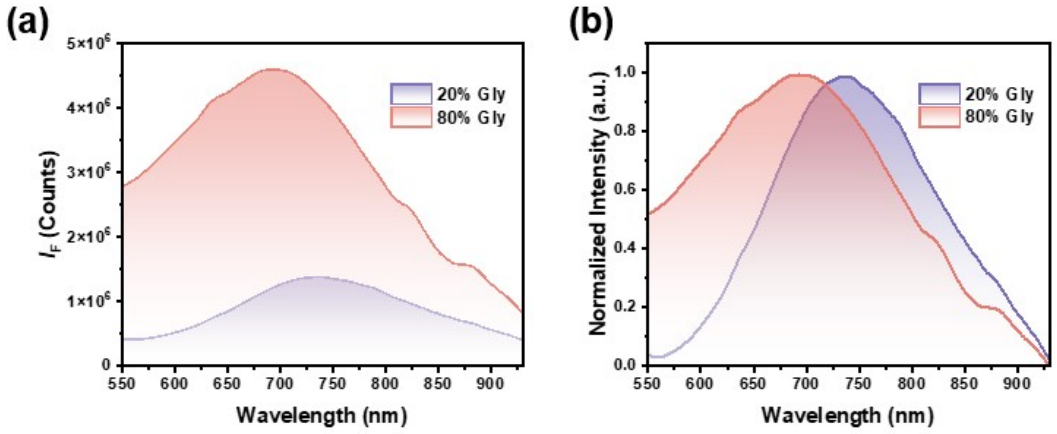

Figure S17. (a)The PL spectra of **DT-NIO** (1×10^{-5} M, λ_{ex} = 430 nm) in methanol–glycerol mixture. (b) The normalized PL spectra of **DT-NIO** in methanol–glycerol mixture.

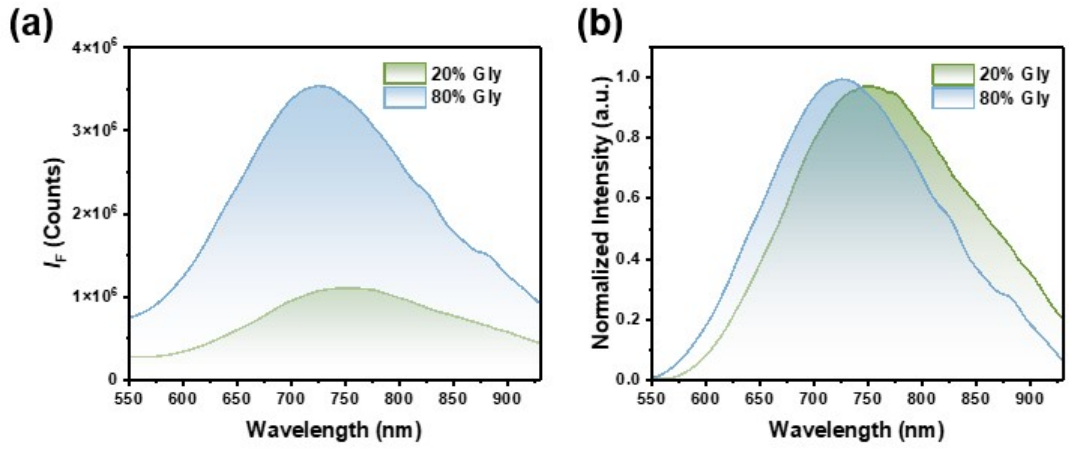

Figure S18. (a)The PL spectra of **DT-NINI** (1×10^{-5} M, λ_{ex} = 430 nm) in methanol–glycerol mixture. (b) The normalized PL spectra of **DT-NINI** in methanol–glycerol mixture.

a control probe bearing a D–A scaffold and structurally similar to **DT-NIN** (**T-NIN**, structure shown in Figure S19) was synthesized. As shown in Figure S19a, although the PL maximum (λ_{PL}) of **T-NIN** in 1,4-dioxane/THF (1:1, v/v) is similar to that of **DT-NIN** in 1,4-dioxane, the PL spectral width of **T-NIN** is slightly broader, indicating its lower scaffold rigidity compared to **DT-NIN**.

To further investigate the effect of viscosity on the PL intensity of **T-NIN**, we initially carried out PL measurements in a methanol/glycerol mixture containing 20% glycerol. However, the recorded PL spectrum of **T-NIN** was abnormally broad (Figure S19b), which we attribute to the poor solubility of **T-NIN** in this solvent mixture.

We therefore turned to a less polar mixed solvent system using paraffin oil (PO) as the high-viscosity component, ensuring good solubility for both **T-NIN** and **DT-NIN**. As shown in Figures S19c and S19d, while the PL intensity of **DT-NIN** is nearly unaffected by viscosity, that of **T-NIN** is markedly enhanced in a solvent of similar polarity (judged by the similar λ_{PL} in the two systems) but higher viscosity (ethyl acetate *vs*. PO/dichloromethane, 6:4, v/v). Accordingly, the D_2–A molecular skeleton exhibits greater scaffold rigidity than its D–A counterpart, demonstrating better resistance to viscosity-induced interference in PL intensity.

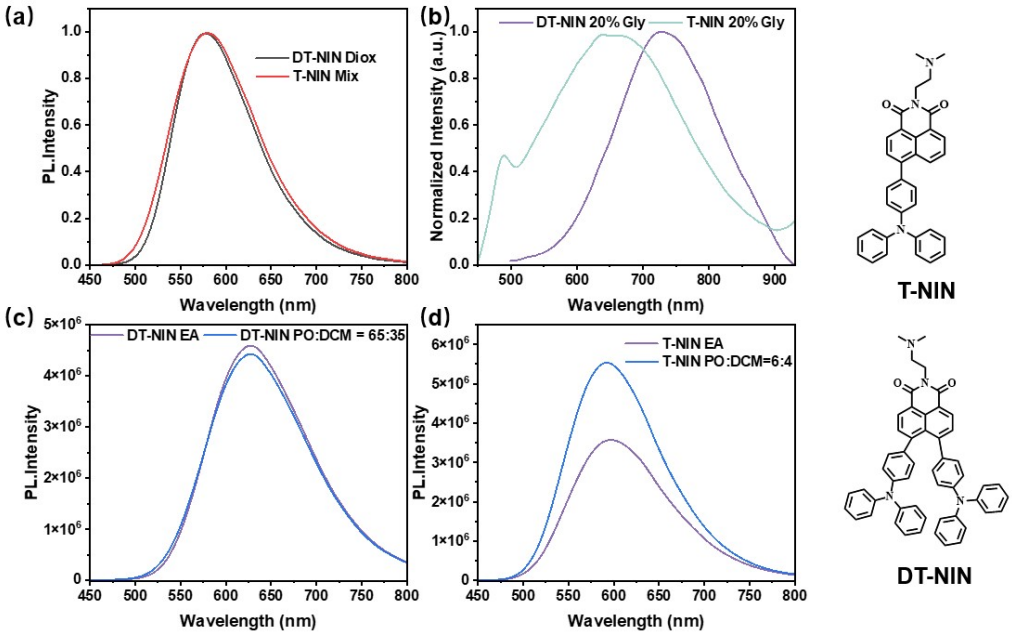

Figure S19. Comparison on scaffold rigidity between probes bearing a D_2–A (**DT-NIN**) and a D–A (**T-NIN**) structure. (a) Normalized PL spectra of **DT-NIN** in 1,4-dioxane and **T-NIN** in a 1,4-dioxane/THF (1:1, v/v) mixture. (b) Normalized PL spectra of **DT-NIN** and **T-NIN** in a methanol/glycerol mixture containing 20% glycerol. (c) PL spectra of **DT-NIN** in ethyl acetate (EA) and PO (paraffin oil)/dichloromethane (DCM) (65:35, v/v) mixture. (d) PL spectra of **T-NIN** in EA and PO/DCM (6:4, v/v) mixture.

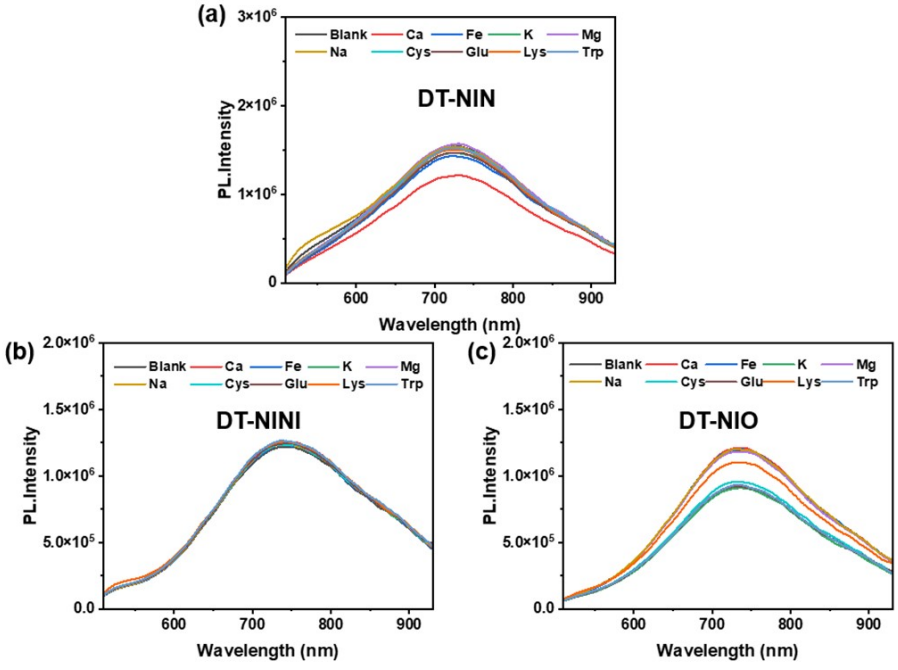

Figure S20. Anti-cross-interference performance of **DT-NIs**. PL spectra of **DT-NIs** (10 μM in

CH_3OH/H_2O = 4:1, v/v) in the presence of various interferents (1.0 mM). (a) **DT-NIN**; (b) **DT-NINI**; (c) **DT-NIO**. Abbreviations: Ca = $CaCl_2$; Fe = $FeSO_4$; K = KCl; Mg = $MgCl_2$; Na = NaCl; Cys = cysteine; Glu = glutamic acid; Lys = lysine; Trp = tryptophan.

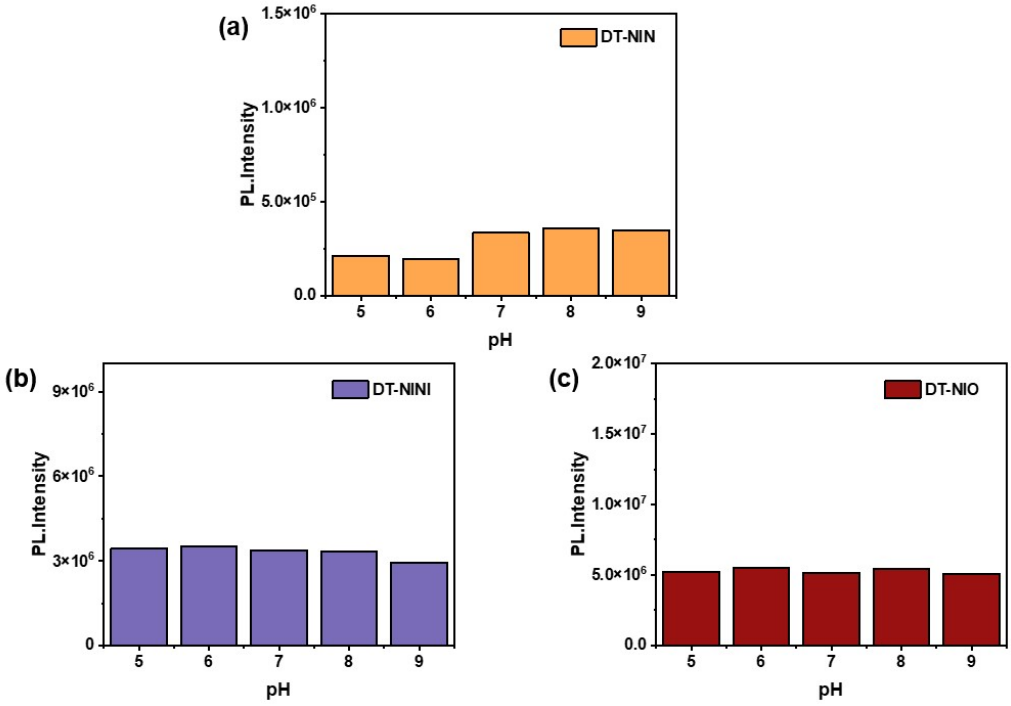

Figure S21. pH-dependent fluorescence stability of the **DT-NIs** series. Influence of pH (5.0-9.0) on the fluorescence intensity of (a) **DT-NIN**, (b) **DT-NINI**, and (c) **DT-NIO** in $CH_3OH:H_2O$ = 1:1.

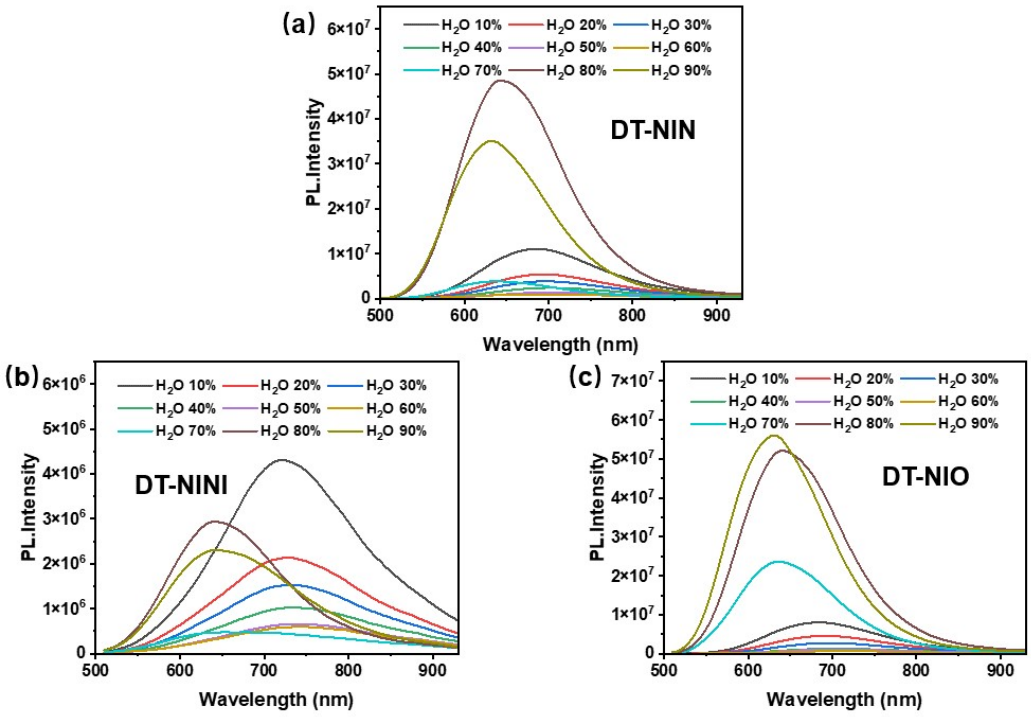

Figure S22. PL properties of **DT-NIs** (10 μM) in THF/H_2O mixtures with various water fractions

(f_w). (a) **DT-NIN**, (b) **DT-NINI**, and (c) **DT-NIO**.

The aggregation-induced emission (AIE) properties of the three **DT-NI** derivatives were evaluated by varying the water fraction (f_w) in H_2O/THF mixed solvents. As shown in Figures S22a and S22c, when f_w increases from 10% to 60%, the PL spectra of both **DT-NIN** and **DT-NIO** exhibit a gradual bathochromic shift accompanied by a decrease in PL intensity. This response can be attributed to the polarity sensitivity of the two probes, indicating that aggregation does not dominate even at f_w up to 60%. Only when f_w reaches 70% do the PL spectra of the two probes begin to blue-shift, along with an increase in PL intensity, suggesting partial aggregation. Upon further increasing f_w to 80% and 90%, the PL intensity of the both probes rises significantly. Since the PL intensity of the two probes at high f_w exceeds their initial intensity at f_w of 10%, both probes exhibit AIE behavior at relatively high f_w.

For **DT-NINI**, no obvious aggregation is observed at f_w ≤60%. Although upon increasing f_w to 70-90%, a similar spectral blue-shift together with recovery of PL intensity is observed, the PL intensity does not exceed the initial value at f_w = 10%, indicating that **DT-NINI** does not possess a pronounced AIE character.

Taken together, **DT-NIN** and **DT-NIO** exhibit AIE character only at f_w ≥ 70%, whereas **DT-NINI** does not display a pronounced AIE feature. Given that under physiologically relevant conditions these probes are primarily distributed within lipophilic membrane structures where the local f_w is far below 70%, the AIE effect is expected to exert negligible interference when using them to determine microenvironmental polarity.

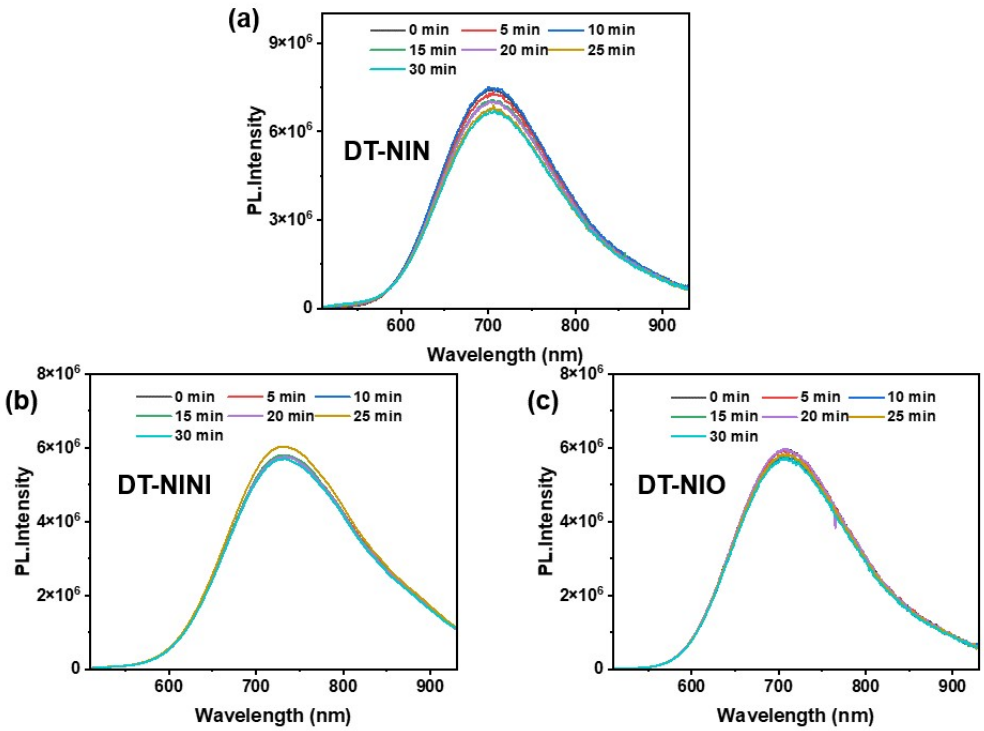

Figure S23. Photostability of **DT-NIs**. PL spectra of **DT-NIs** (10 μM in *N*,*N*-dimethylformamide) upon continuous irradiation with a blue LED (2 W, λ = 405 nm) over different time intervals (0-30 min). (a) **DT-NIN**; (b) **DT-NINI**; (c) **DT-NIO**.

2.4 Biological experiment

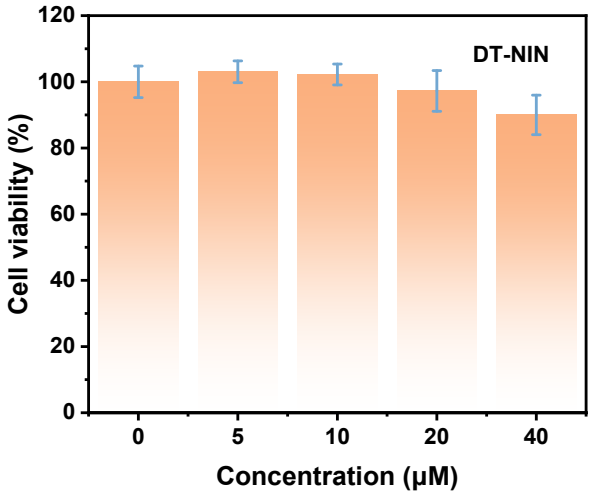

Figure S24. Cell viability of L929 cells after incubation with different concentrations of **DT-NIN** (0−40 μM) after 24 h incubation. Values were expressed as mean ± SD (n = 5).

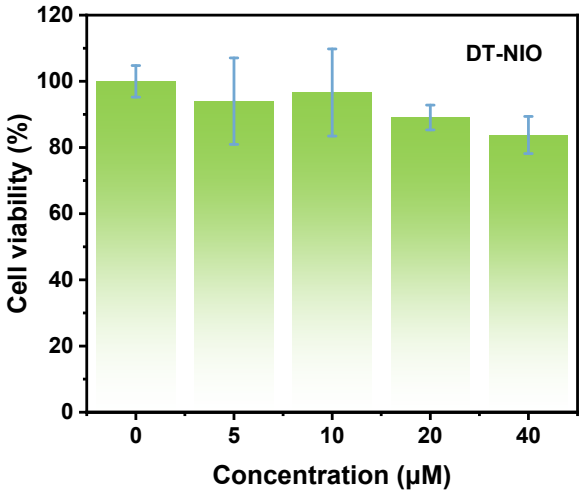

Figure S25. Cell viability of L929 cells after incubation with different concentrations of **DT-NIO** (0−40 μM) after 24 h incubation. Values were expressed as mean ± SD (n = 5).

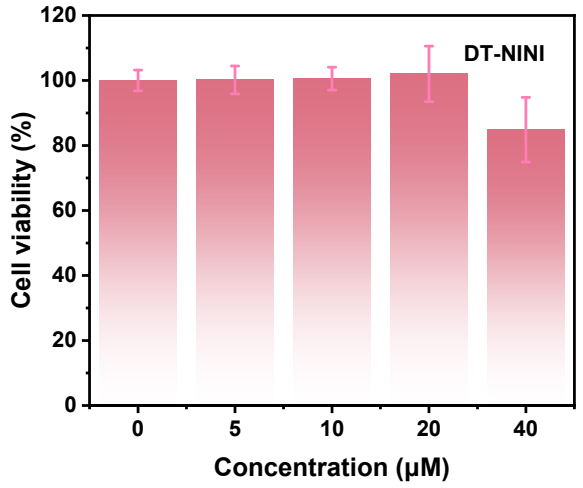

Figure S26. Cell viability of L929 cells after incubation with different concentrations of **DT-NINI** (0−40 μM) after 24 h incubation. Values were expressed as mean ± SD (n = 5).

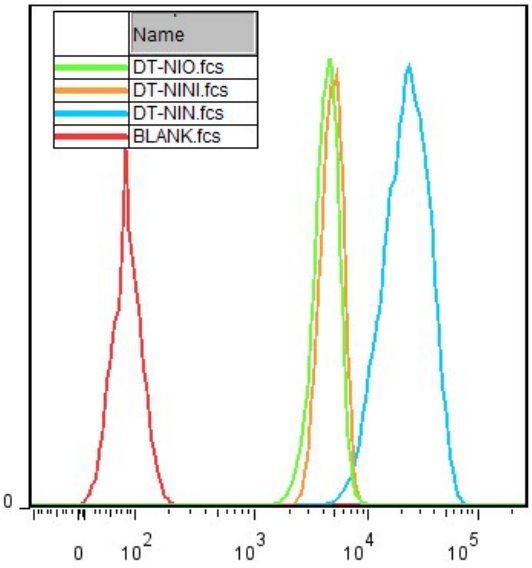

Figure S27. Flow cytometric results of **DT-NIN, DT-NIO** and **DT-NINI** in L929 cells. The results showed that all of these molecules could be applied as fluorescent probe in living cells tracing.

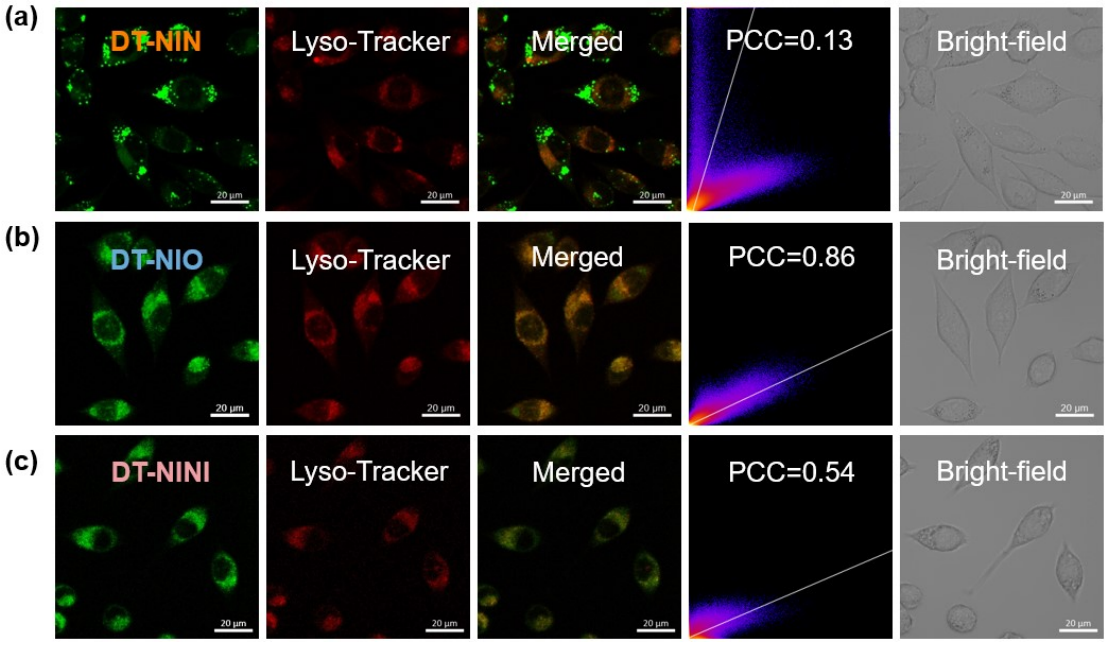

Figure S28. Co-localization analysis of **DT-NIs** with Lyso-Tracker. (a) Confocal microscopy fluorescence images of L929 cells co-labeled with for **DT-NIN** (10 μM) for 3 h and commercial organelle trackers (0.2 μM) for 30 min. (b) Confocal microscopy fluorescence images of L929 cells co-labeled with for **DT-NIO** (c) Confocal microscopy fluorescence images of L929 cells co-labeled with for **DT-NINI**. Red channel: Lyso-tracker (0.2 μM, $\lambda_{ex}/\lambda_{em}$ = 543/548−650 nm). Green channel: **DT-NIs**: $\lambda_{ex}/\lambda_{em}$ = 405/600−740 nm.

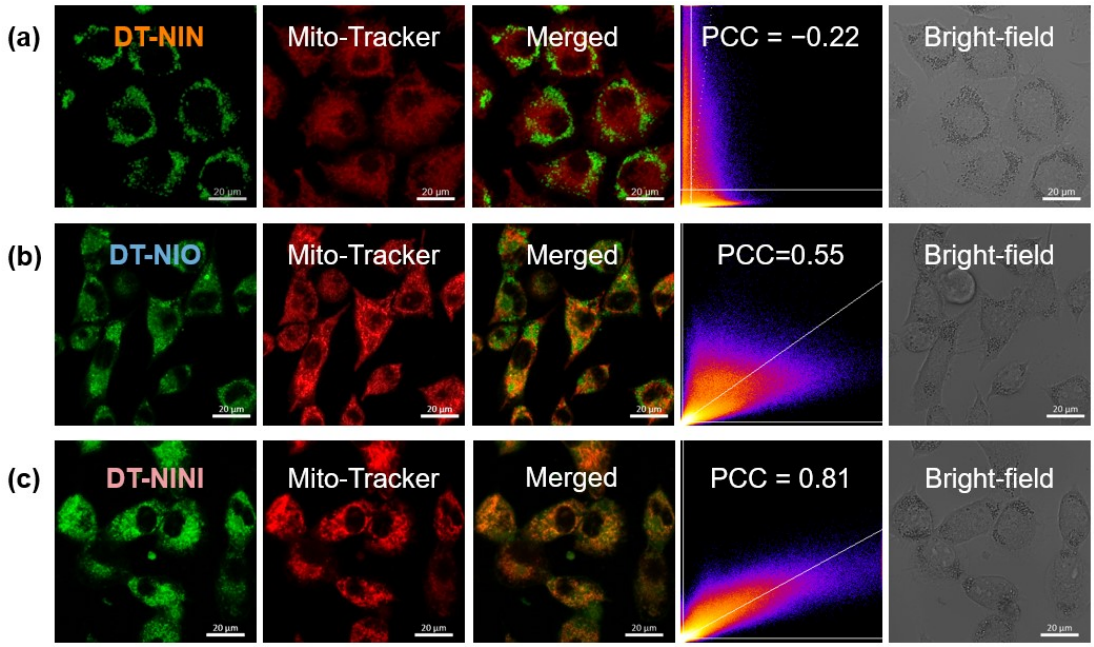

Figure S29. Co-localization analysis of **DT-NIs** with Mito-Tracker. (a) Confocal microscopy fluorescence images of L929 cells co-labeled with for **DT-NIN** (10 μM) for 3 h and commercial organelle trackers (0.2 μM) for 30 min. (b) Confocal microscopy fluorescence images of L929 cells co-labeled with for **DT-NIO** (c) Confocal microscopy fluorescence images of L929 cells co-labeled with for **DT-NINI**. Red channel: Mito-tracker (0.2 μM, $\lambda_{ex}/\lambda_{em}$ = 633/638−759 nm). Green channel: **DT-NIs**: $\lambda_{ex}/\lambda_{em}$ = 405/600−740 nm.

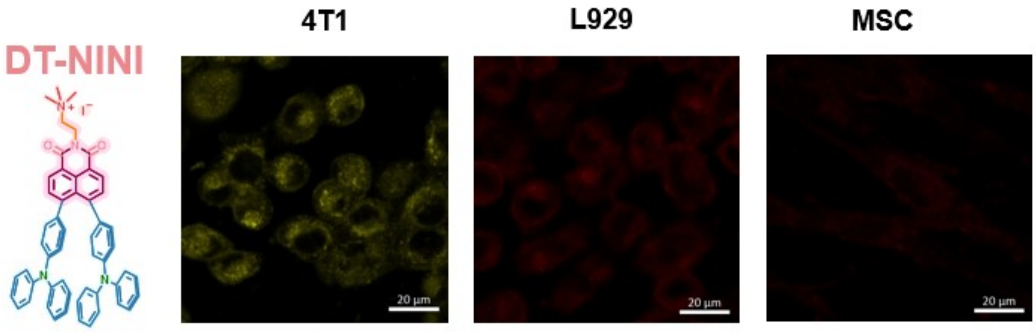

Figure S30. Confocal fluorescence images of 4T1, L929 and MSC cells co-stained with **DT-NINI** ($\lambda_{ex}/\lambda_{em}$ = 405/600−740 nm).

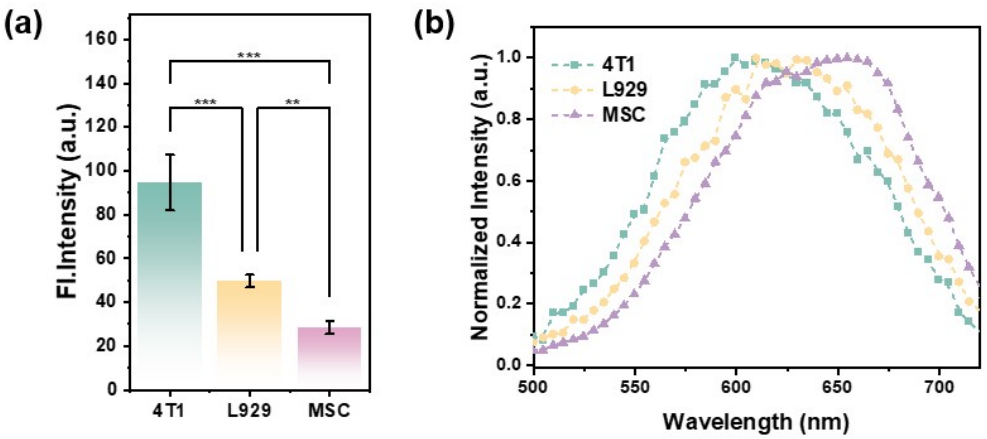

Figure S31. PL intensity and spectra of **DT-NINI** (10 μM) in cells (λ_{ex} = 405 nm, λ_{em} = 600−740 nm). (a) Average I_F of **DT-NINI** in 4T1, L929 and MSC cells. The data are shown as mean ± SD (n = 5), $^{**}P < 0.01$, $^{***}P < 0.001$. (b) Normalized PL spectra of **DT-NINI** in 4T1, L929 and MSC cells.

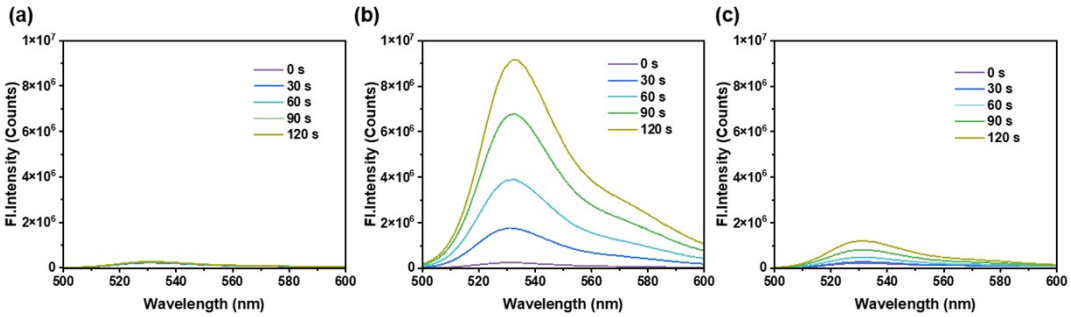

Figure S32. Fluorescence intensity of DCFH at 525 nm (λ_{ex} = 488 nm) as a function of irradiation time (0-120 s) in the presence of DCFH (a), **DT-NINI** + DCFH (b) and **DT-NIN** + DCFH (c).

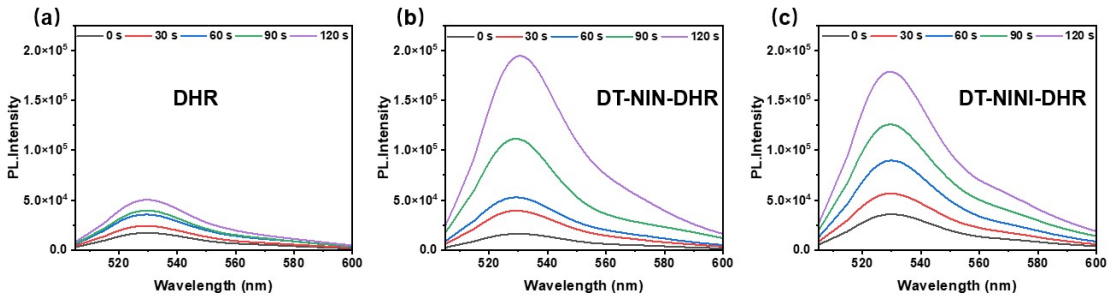

Figure S33. PL intensity of DHR in the presence or absence of **DT-NIN** or **DT-NINI** as a function of irradiation time (0-120 s). (a) DHR (10 μM); (b) DHR (10 μM) + **DT-NIN** (10 μM); and (c) DHR (10 μM) + **DT-NINI** (10 μM). (λ_{ex} = 480 nm)

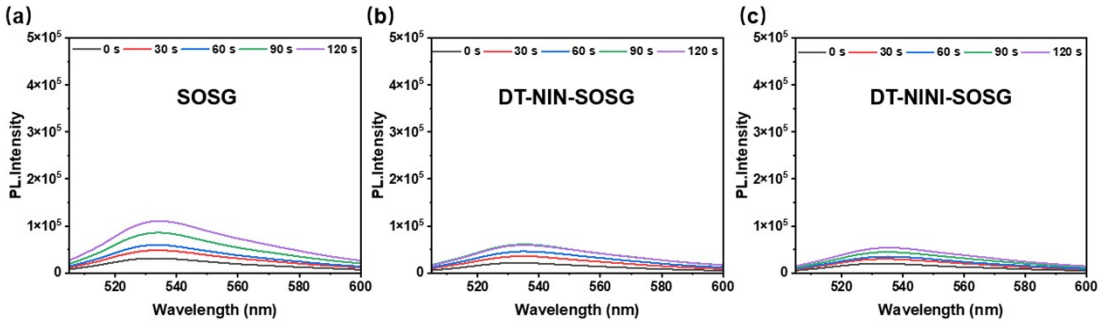

Figure S34. PL intensity of SOSG in the presence or absence of **DT-NIN** or **DT-NINI** as a function of irradiation time (0-120 s). (a) SOSG (10 μM); (b) SOSG (10 μM) + **DT-NIN** (10 μM); and (c) SOSG (10 μM) + **DT-NINI** (10 μM). (λ_{ex} = 480 nm)

3. Copies of NMR and HR-MS spectra of compounds

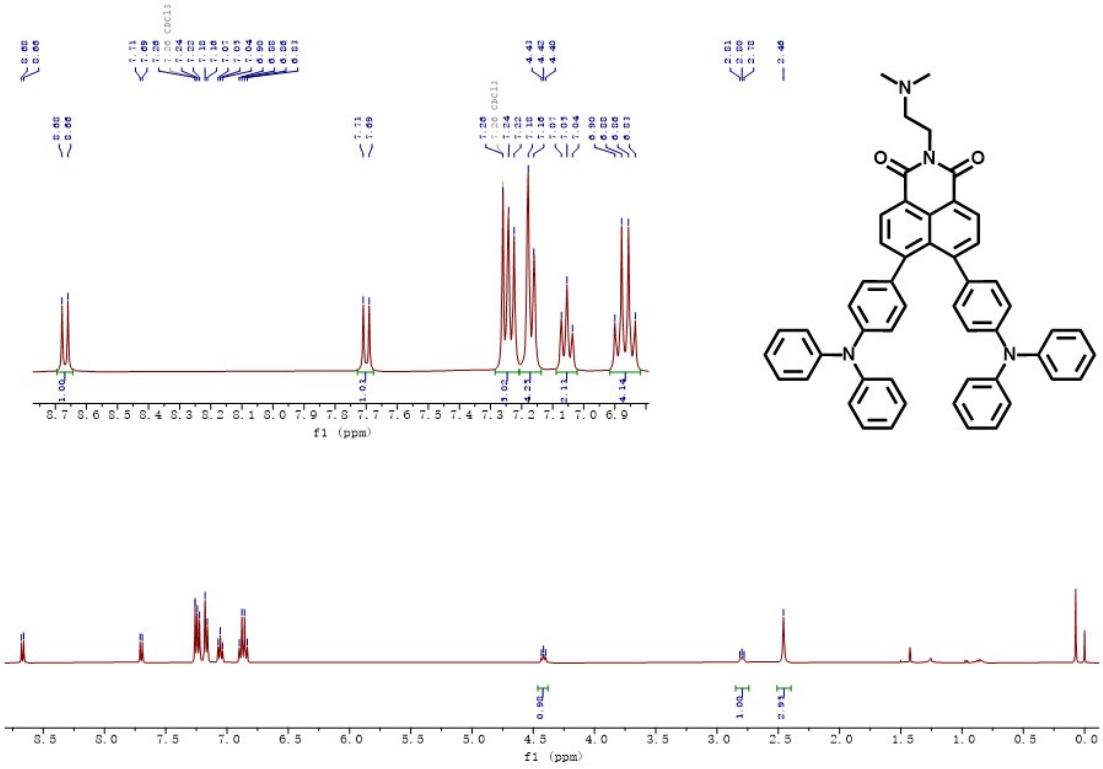

Figure S35. The ^{1}H NMR spectra of **DT-NIN** in $CDCl_3$.

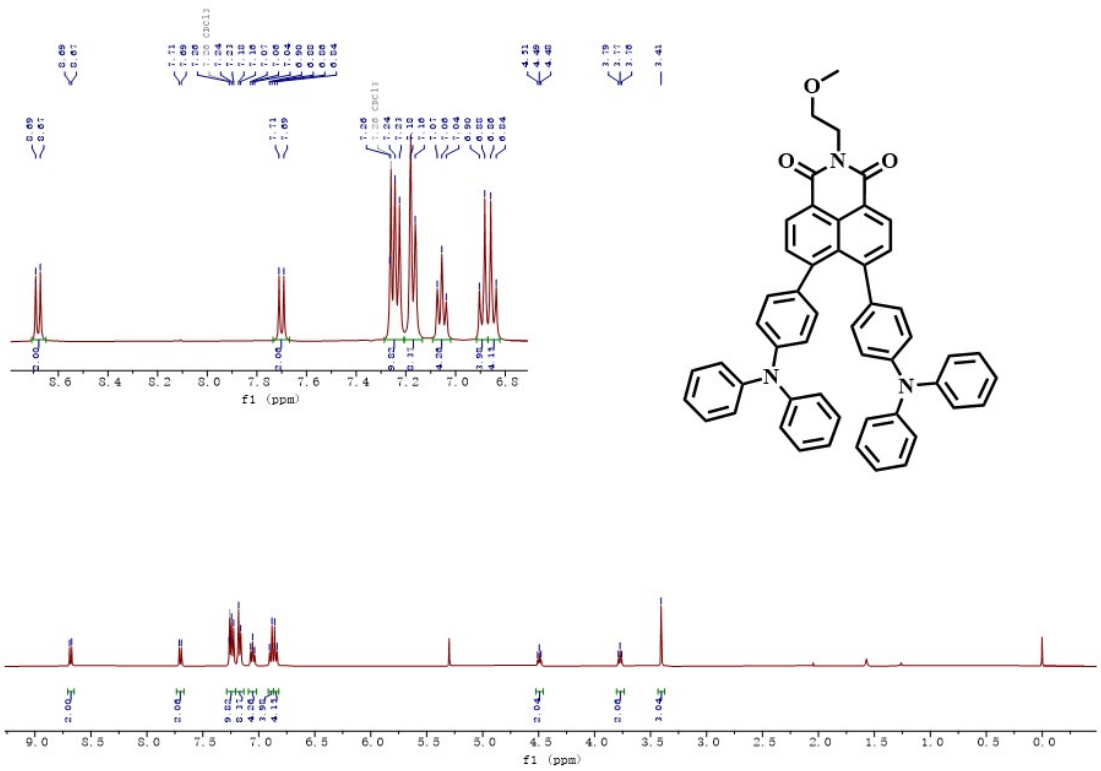

Figure S36. The ^{1}H NMR spectra of **DT-NIO** in $CDCl_3$.

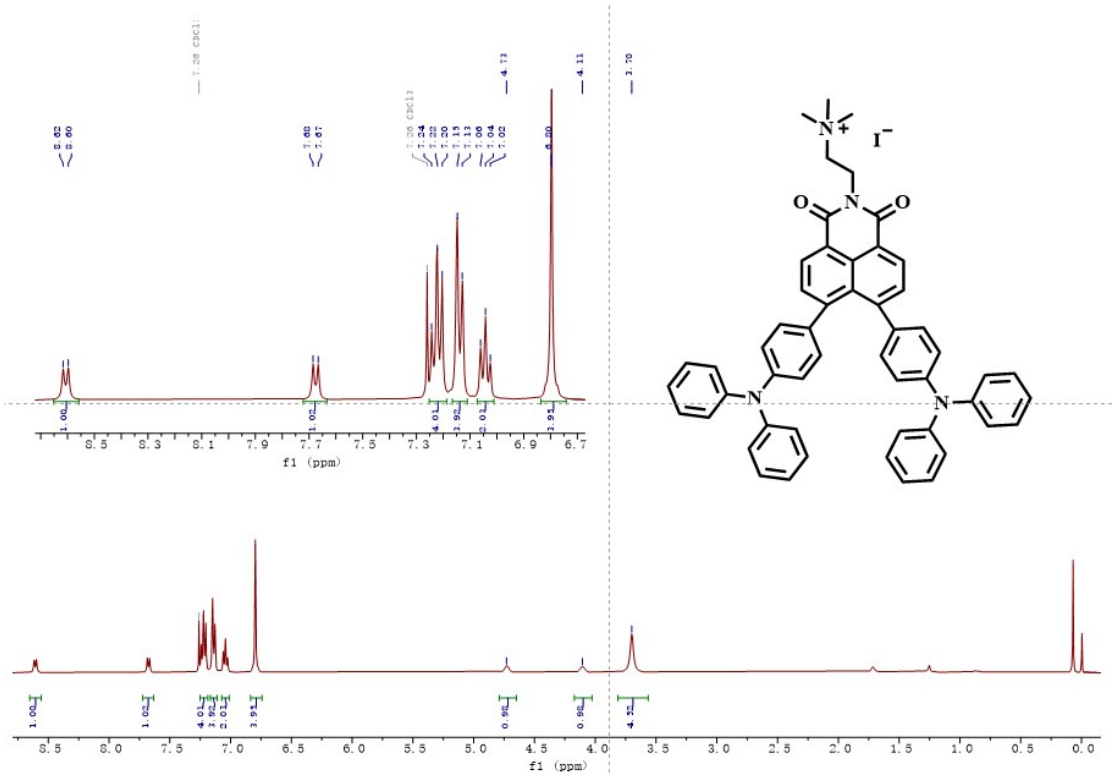

Figure S37. The ^{1}H NMR spectra of **DT-NINI** in $CDCl_3$.

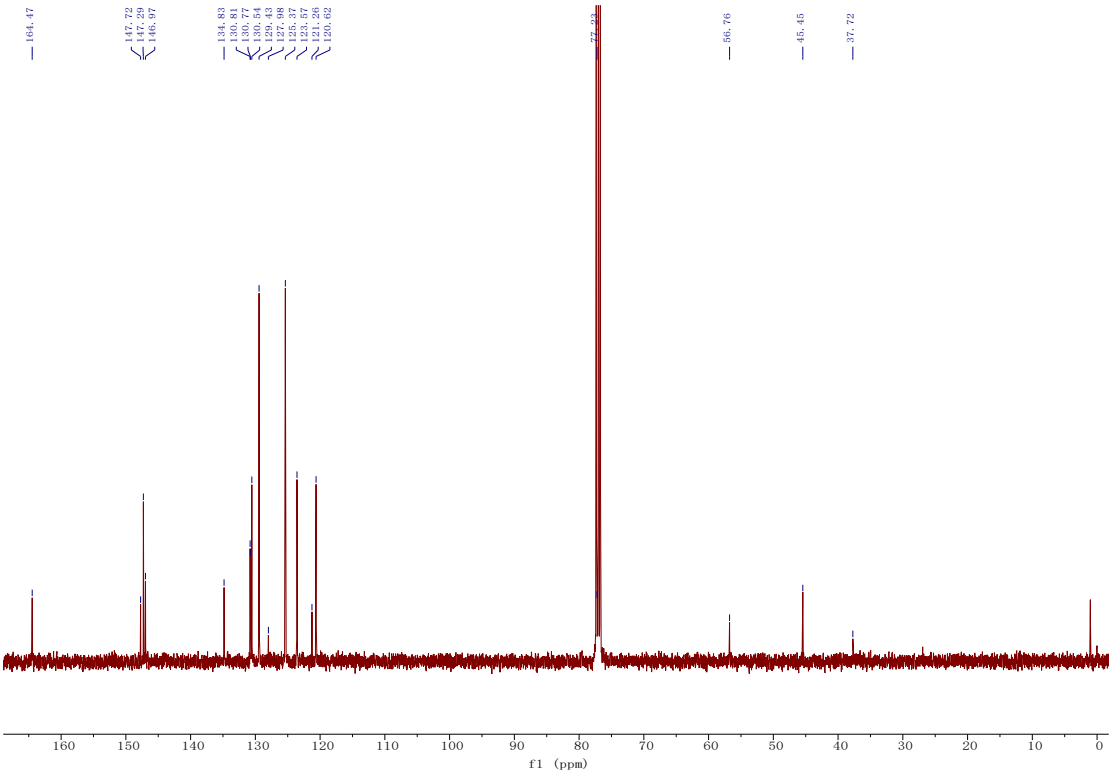

Figure S38. The ^{13}C NMR spectra of **DT-NIN** in $CDCl_3$.

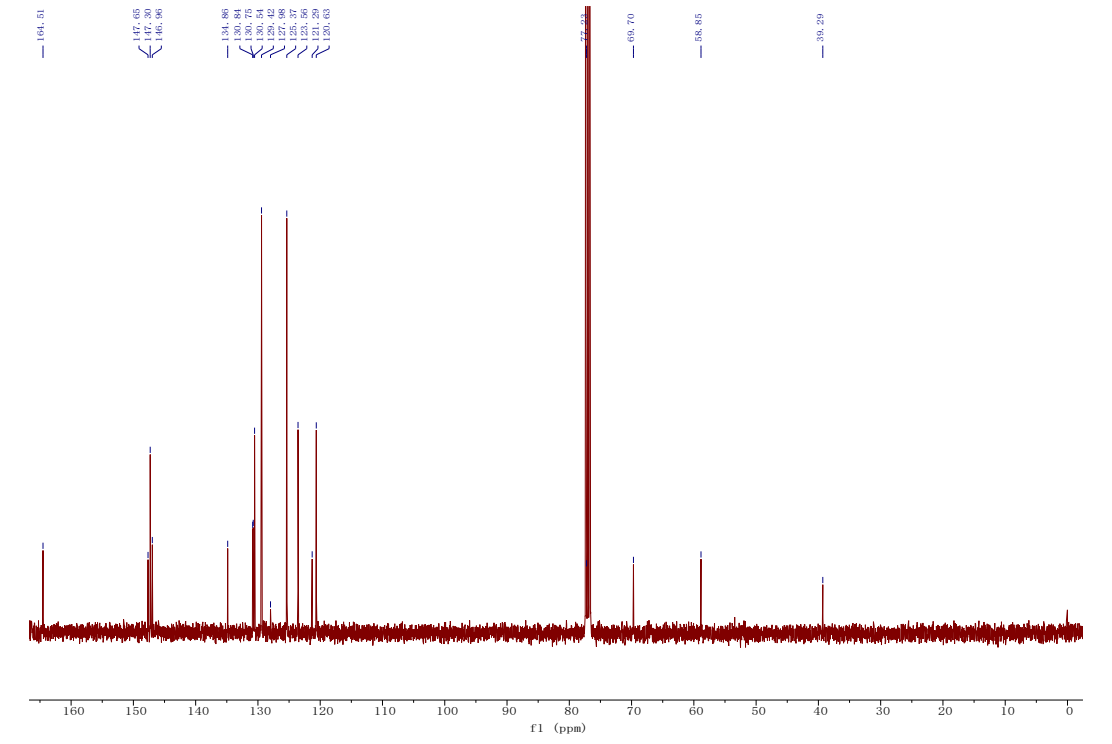

Figure S39. The ^{13}C NMR spectra of **DT-NIO** in $CDCl_3$.

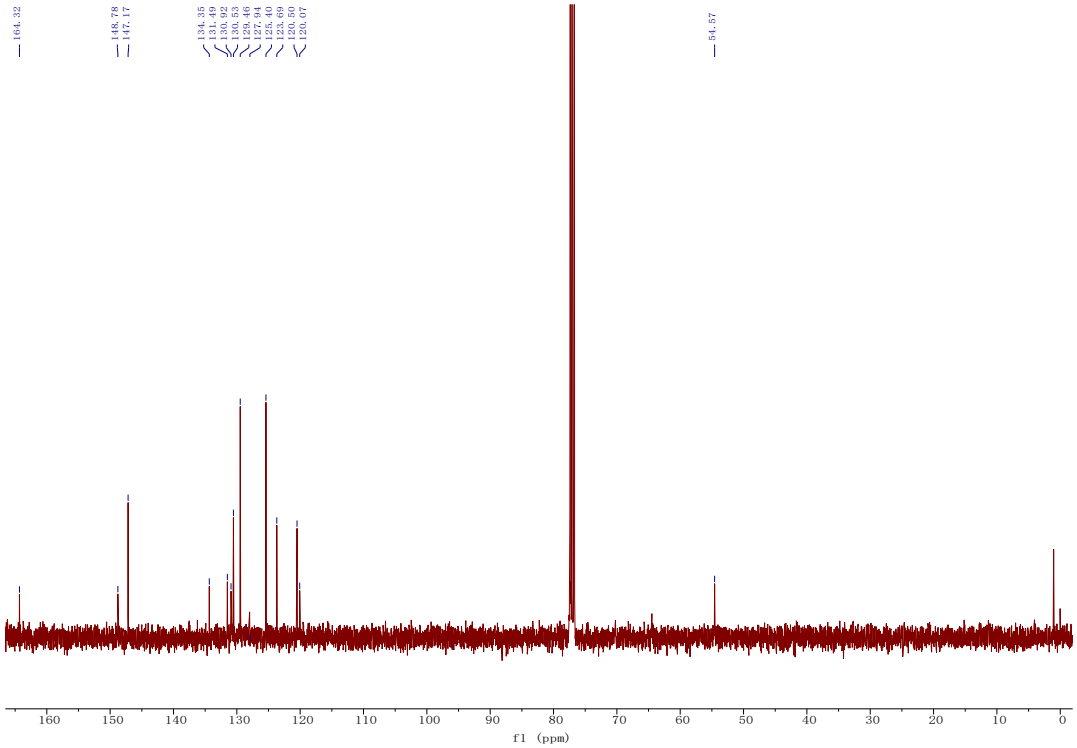

Figure S40. The ^{13}C NMR spectra of **DT-NINI** in $CDCl_3$.

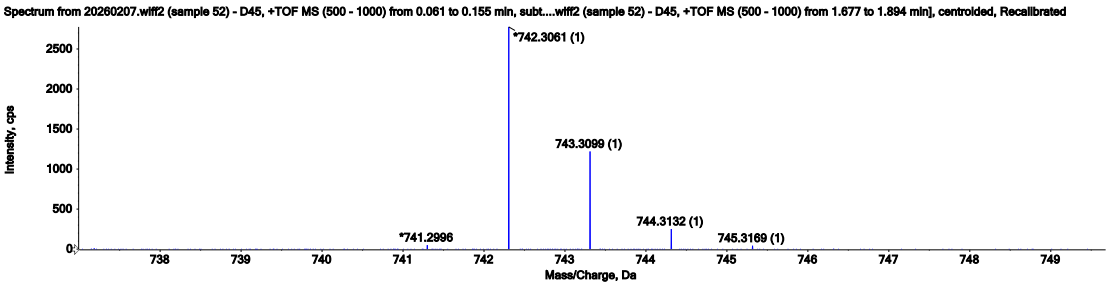

Figure S41. HR-MS spectrum of **DT-NIO**.

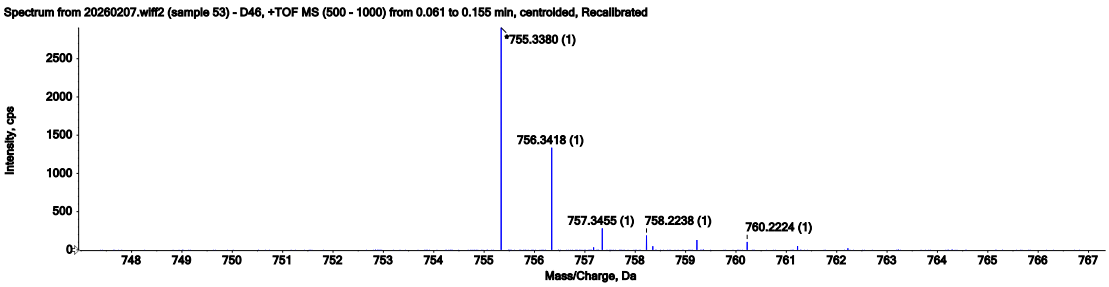

Figure S42. HR-MS spectrum of **DT-NIN**.

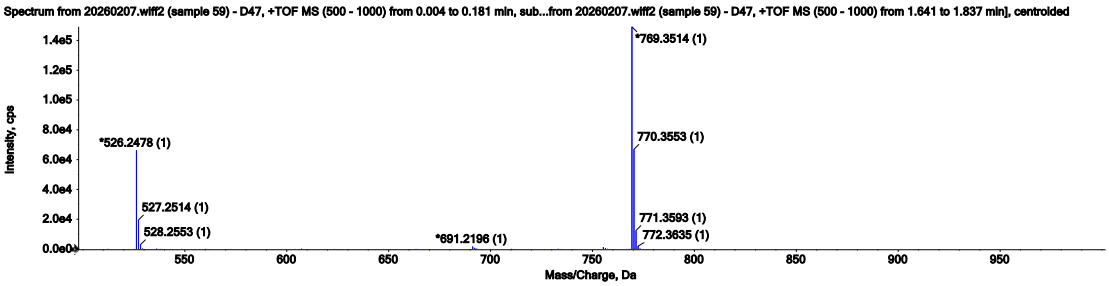

Figure S43. HR-MS spectrum of **DT-NINI**.

Table S3. Crystal data and structure refinements of **DT-NIN**.

Empirical formula	$C_{52}H_{42}N_4O_2$
Formula weight	754.89
Temperature/K	186.0
Crystal system	monoclinic
Space group	P2/c
a/Å	17.3338(11)
b/Å	9.6343(7)
c/Å	26.5027(17)
α/°	90
β/°	107.145(2)
γ/°	90
Volume/Å^3	4229.2(5)
Z	4
ρ_{calc}g/cm^3	1.186
μ/mm^{-1}	0.073
F(000)	1592.0
Crystal size/mm^3	0.32 × 0.18 × 0.02
Radiation	MoKα (λ = 0.71073)
2Θ range for data collection/°	4.228 to 49.998

Index ranges	$-20 \le h \le 20, -11 \le k \le 11, -29 \le l \le 31$
Reflections collected	68209
Independent reflections	7380 [R_{int} = 0.1565, R_{sigma} = 0.0914]
Data/restraints/parameters	7380/143/565
Goodness-of-fit on F^2	1.153
Final R indexes [I>=2σ (I)]	R_1 = 0.0891, wR_2 = 0.2257
Final R indexes [all data]	R_1 = 0.1415, wR_2 = 0.2668
Largest diff. peak/hole / e $Å^{-3}$	0.68/-0.27

4. Reference

(1) Zhang, J.; Lu, T. *Phys. Chem. Chem. Phys.* **2021**, *23* (36), 20323–20328.